Dynamic Field Map Estimation Using a Spiral-In/ Spiral-Out Acquisition

Bradley P. Sutton[1]*, Douglas C. Noll[1], Jeffrey A. Fessler[1]

[1]Dept. of Biomedical Engineering, University of Michigan

July 3, 2003

dynamic field map estimation

Address correspondence to:

Brad Sutton

1073 BIRB, 2360 Bonnisteel

Ann Arbor, MI 48109–2108

bpsutton@umich.edu

(734) 647-1996   FAX:(734) 936-4218

Abstract

The long readout times of single-shot acquisitions and the high field strengths desired for functional MRI using blood-oxygenation level dependent (BOLD) contrast make functional scans sensitive to magnetic field inhomogeneity. If not corrected during image reconstruction, field inhomogeneity can cause geometric distortions in the images when Cartesian k-space trajectories are used and blurring with spiral acquisitions. Many traditional methods to correct for field inhomogeneity distortions rely on a static field map that was measured using images that are themselves distorted. In this work, we propose a regularized least-squares approach to joint estimation of both the undistorted image and field map at each acquisition using a spiral-in/ spiral-out pulse sequence. Simulation and phantom studies show that our method is accurate and stable over a time series. Human functional studies show that the jointly estimated field map may be more accurate than standard field map estimates in the presence of respiration-induced phase oscillations, leading to better detection of functional activation. The proposed method measures a dynamic field map that accurately tracks magnetic field drift and respiration-induced phase oscillations during the course of a functional study.

Keywords: image reconstruction, field inhomogeneity, functional MRI, iterative methods.

1   INTRODUCTION

Functional imaging using blood-oxygenation level dependent (BOLD) contrast is performed by acquiring T_2^*-weighted images using gradient-echo acquisitions during task and rest [1]. The gradient-echo acquisitions typically are fast, single-shot techniques such as EPI or spirals. Single-shot techniques allow high temporal resolution and avoid the mixing of respiratory phases or subject motion between the shots in a multi-shot acquisition. However, the long readout times of single-shot acquisitions make them sensitive to magnetic field inhomogeneities that can lead to severe distortions in the images. Magnetic field inhomogeneities exist around regions where materials with different magnetic susceptibility come into contact, for example at air/tissue interfaces. When uncorrected, these effects can cause geometric distortions when EPI scans are used and blurring with spiral acquisitions. The artifacts due to field inhomogeneity can cause problems when obtaining functional results from areas near air/tissue interfaces. Spatial distortions can also degrade the accuracy of registering images from different time points for motion correction and registering functional results to anatomical scans.

Many image reconstruction methods have been proposed to correct for field distortions in spiral imaging, *e.g.* [2, 3, 4, 5, 6]. There are two steps involved in most field inhomogeneity correction schemes. The first is to measure the spatial variation of the magnetic field, this is referred to as estimating a field map. The second step is to use that field map to compensate for field inhomogeneities during the reconstruction. Some methods have been presented that by-pass the first step, for example Noll *et al.* [3] use an auto-focusing criteria based on the assumption that the phase is locally smoothly varying in a field-corrected image. However, most field correction methods rely on obtaining a good estimate of the field map.

Conventionally, the field map is measured by acquiring two images at slightly different echo times and dividing their phase difference by the difference in echo times [7]. That method assumes implicitly that all of the off-resonance phase accrual occurs at the echo time, ignoring dephasing during the data readout which may be longer than the echo time. If the images used to measure the field map are taken with the same acquisition parameters that are to be used in the imaging study, then they are distorted by field inhomogeneities and the resulting field map suffers from the image distortions. A multi-shot, short echo time scan can be used to obtain a less-distorted field map, but such field maps require extra acquisitions and may suffer from mixing of respiratory and cardiac phases [8].

For standard field map estimation, the echo time of the two reference images must be within a few milliseconds of each other to avoid ambiguity in the field map measurement that would result from 2π phase wraps. Given that the total acquisition time for an single-shot image is tens of milliseconds, one must use two separate acquisitions (TR intervals) to acquire two images with slightly different echo times. Respiration-induced phase variations in the two reference images, other physiological noise, or subject motion between the two scans can lead to errors in the standard field map estimate. For example, in our scans, the center frequency of an axial slice can vary by 1 Hz depending on the position in the respiratory cycle. This could result in a phase difference of as much as $(2\pi\mathrm{TE} \times 1\ \mathrm{Hz})$radians between the two acquisitions even in the absence of additional field inhomogeneity. This phase difference divided by the difference in echo times would induce a 15 Hz error in the field map estimate for an echo time of 30 ms and a echo time delay of 2 ms. Using the spiral-in/ spiral-out sequence along with our proposed joint estimation algorithm, we are able to estimate the field map during one TR interval. The spiral-in sequence is followed by a short rest or gap of 1 ms before the spiral-out portion of the sequence is executed. Section 4.4 gives an example showing that the standard field map estimation technique is not

applicable to field map estimation using the spiral-in and spiral-out images within a single acquisition.

Field maps resulting from standard estimates are usually assumed to be static over the course of the functional study because an additional scan with a delayed echo time is required. This additional scan is usually performed at the beginning or the end of a functional study. This one measured field map is used for correcting the entire time series of images. Dynamic changes in the field map for a slice can occur during the course of a functional study. These changes can be due to respiratory-cycle induced phases, main field drift, and subject motion. When field-corrected image reconstruction algorithms are used, these dynamic changes can lead to further distortions in the images for a time series. Nayak *et al.* presented a method to form standard, dynamic estimates of a low-resolution field map by delaying echo times of subsequent shots in a multi-shot experiment [9, 10]. However, these estimates are sensitive to the differences in reference images discussed in the previous paragraph, whereas the method we propose here will estimate the field map within a single acquisition.

This paper describes a new way to combine the two steps used for field inhomogeneity correction used in conjunction with a certain pulse sequence. We propose to reconstruct an undistorted image and its associated, dynamic, undistorted field map from a spiral-in/ spiral-out acquisition. This method retains the time resolution and other benefits of single-shot methods while correcting for distortions caused by the changing field map. The spiral-in/ spiral-out pulse sequence can acquire the same number of slices per TR as a spiral-out sequence [11] and therefore should not change the setup of current fMRI studies. By measuring the field map during each acquisition of a slice, we are able to track and compensate for dynamic changes in the field map.

In Section 2, we derive our nonlinear least-squares joint field map and image estimation algorithm and discuss some implementation issues. Our field-inhomogeneity-corrected image reconstruction method was discussed in [12] which included methods to speed computation: time segmentation and the Nonuniform Fast Fourier Transform (NUFFT) [13]. Both of those methods are used extensively in this work. Simulation, phantom, and human data experiments are described in Section 3 with the results given in Section 4.

2 Theory

We approach the simultaneous estimation problem by forming a cost function based on the signal equation for MRI and then minimizing it over the image and field map simultaneously. Section 2.1 presents our cost function based on the signal equation in terms of the unknown image and field map. Section 2.2 discusses our minimization process.

2.1 Nonlinear Least-Squares Joint Estimation

In MRI, the equation for the complex baseband signal, ignoring relaxation effects, is given by,

$$s(t) = \int f(\boldsymbol{r}) e^{-i\omega(\boldsymbol{r})t} e^{-i2\pi(\boldsymbol{k}(t)\cdot\boldsymbol{r})} d\boldsymbol{r}, \tag{1}$$

where $s(t)$ is the signal at time t during the readout, $f(\boldsymbol{r})$ is a function of the object's transverse magnetization at location $\boldsymbol{r}$, $\omega(\boldsymbol{r})$ is the field inhomogeneity, and $\boldsymbol{k}(t)$ is the k-space trajectory. In an MR scan, the raw measurements are noisy samples of this signal,

$$y_m = s(t_m) + \varepsilon_m, \quad m = 1, \ldots, M, \tag{2}$$

and from these samples we would like to simultaneously estimate the image, $f(\boldsymbol{r})$, and the field map, $\omega(\boldsymbol{r})$.

This is clearly an ill-posed problem since there is an infinite collection of solutions, $f(\boldsymbol{r})$ and $\omega(\boldsymbol{r})$, that closely match the data $\boldsymbol{y} = (y_1, \ldots, y_m)$. We proceed by parameterizing the object and field map in terms of basis functions as follows:

$$\begin{aligned} f(\boldsymbol{r}) &\approx \sum_{n=0}^{N-1} f_n \phi_1(\boldsymbol{r} - \boldsymbol{r}_n) \\ \omega(\boldsymbol{r}) &\approx \sum_{n=0}^{N-1} \omega_n \phi_2(\boldsymbol{r} - \boldsymbol{r}_n). \end{aligned} \tag{3}$$

For the results presented in this paper, we will use the voxel indicator function: $\phi_1(\boldsymbol{r}) = \phi_2(\boldsymbol{r}) = \text{rect}(r_1/\Delta_{r_1}) \cdots \text{rect}(r_P/\Delta_{r_P})$ for the P-dimensional problem. This choice is natural for the object, $f(\boldsymbol{r})$, since the display device will use square areas of nearly constant luminance, but better choices for the field map, $\omega(\boldsymbol{r})$, may exist that would allow for the modeling of within-voxel nonuniformity of the

magnetic field intensity. Alternative basis functions will be explored in a future work. Substituting Eq. (3) in Eq. (1), yields

$$s(t) \approx \Phi(\boldsymbol{k}(t)) \sum_{n=0}^{N-1} f_n e^{-i\omega_n t} e^{-i2\pi(\boldsymbol{k}(t)\cdot\boldsymbol{r}_n)}, \tag{4}$$

where $\Phi(\boldsymbol{k}(t))$ results from the Fourier Transform of $\phi(\boldsymbol{r})$, *i.e.* $\mathrm{sinc}(k_1(t)\Delta_{r_1})\cdots\mathrm{sinc}(k_P(t)\Delta_{r_P})$. We express the noisy measured samples of this signal in matrix-vector form as follows

$$\boldsymbol{y} = \boldsymbol{A}(\boldsymbol{\omega})\boldsymbol{f} + \boldsymbol{\varepsilon}, \tag{5}$$

where $\boldsymbol{f} = (f_0, \ldots, f_{N-1})$ and the elements of the $M \times N$ matrix $\boldsymbol{A}(\boldsymbol{\omega})$ are

$$a_{m,n}(\boldsymbol{\omega}) = \Phi(\boldsymbol{k}(t_m)) e^{-i\omega_n t_m} e^{-i2\pi\boldsymbol{k}(t_m)\cdot\boldsymbol{r}_n}. \tag{6}$$

Our goal is to estimate the image, $\boldsymbol{f}$, and the field map, $\boldsymbol{\omega}$, from the k-space data $\boldsymbol{y}$, accounting for the statistics of the noise $\boldsymbol{\varepsilon}$.

In [12], we used the formulation in Eq. (5) as part of an inverse problem approach to field-inhomogeneity corrected image reconstruction, *i.e.* estimate the image $\boldsymbol{f}$ given the field map, $\boldsymbol{\omega}$. We showed that in regions with large field inhomogeneity, the iterative reconstruction method results in more accurate images than the standard conjugate phase approach. However, this accuracy may be limited by errors in the estimated field map. In [12], a static field map from an additional scan was used. Due to the size of the system matrix $\boldsymbol{A}$, directly calculating its inverse is impractical and it is usually ill-conditioned. Instead, we used the iterative method of conjugate gradients (CG). The main operations involved in the CG method are computing $\boldsymbol{A}\boldsymbol{x}$ and $\boldsymbol{A}^\star\boldsymbol{y}$, *i.e.* evaluating Eq. (4) and a complex conjugate transpose version of that equation. We developed fast and accurate approximations to speed the computation of these two matrix-vector products, the non-uniform fast Fourier Transform (NUFFT) [13] and a min-max optimal interpolator for time segmentation [12]. In this work, we propose to estimate both the image and the field map and we will use both of these speed-up methods extensively.

Since the dominant noise in MRI is white Gaussian [14], we can estimate $\boldsymbol{f}$ and $\boldsymbol{\omega}$ by minimizing the following penalized least-squares cost function,

$$\begin{aligned} \Psi(\boldsymbol{f}, \boldsymbol{\omega}) &= \frac{1}{2}\|\boldsymbol{y} - \boldsymbol{A}(\boldsymbol{\omega})\boldsymbol{f}\|^2 + \beta_1 R(\boldsymbol{f}) + \beta_2 R(\boldsymbol{\omega}) \quad \text{so that,} \\ \hat{\boldsymbol{f}}, \hat{\boldsymbol{\omega}} &= \arg\min_{\boldsymbol{f}, \boldsymbol{\omega}} \Psi(\boldsymbol{f}, \boldsymbol{\omega}). \end{aligned} \tag{7}$$

6

The second half of the equation for $\Psi(\boldsymbol{f}, \boldsymbol{\omega})$ includes regularization terms, $R(\boldsymbol{f})$ and $R(\boldsymbol{\omega})$, that penalize the roughness of the estimated image and field map. The parameter β_1 is chosen to control noise but not to significantly affect the resolution of the problem. For the regularization of the field map, β_2 is chosen to result in a relatively smooth field map, similar to the standard field map estimates after smoothing (see Section 3). For simplicity, we used a quadratic regularization, $R(\boldsymbol{f}) = \frac{1}{2}\|\boldsymbol{C}\boldsymbol{f}\|^2$ for a matrix $\boldsymbol{C}$ that takes differences between neighboring pixels.

2.2 Implementation: nonlinear estimation problem

The minimization problem, Eq. (7), requires an iterative algorithm. We alternate between updating $\hat{\boldsymbol{f}}$ and $\hat{\boldsymbol{\omega}}$. First we update the image given the current estimate of the field map, then we update the field map given the new estimate of the image. For updating the image, we exploit the linear relation between the image and the data and apply the iterative conjugate gradient (CG) algorithm for minimization of Eq. (7) over $\boldsymbol{f}$. The CG algorithm, along with the fast methods presented in [12], results in a quick convergence to the best fit image for this part of the algorithm. Once we have updated our estimate of the image, $\hat{\boldsymbol{f}}$, we use gradient descent on the cost function Ψ from Eq. (7) to update the estimate of the field map, $\hat{\boldsymbol{\omega}}$. The gradient of Ψ with respect to $\boldsymbol{\omega}$ is given by:

$$
\begin{aligned}
\frac{\partial}{\partial \omega_n}\Psi(\boldsymbol{\omega}) \;=\; & \frac{1}{2}\sum_{m=1}^{M}\Big(-it_m f_n^{\star}\Phi^{\star}(\boldsymbol{k}(t_m))e^{i(2\pi\boldsymbol{k}(t_m)\cdot\boldsymbol{r}_n+\omega_n t_m)}(y_m - [\boldsymbol{A}(\boldsymbol{\omega})\boldsymbol{f}]_m) \\
& + \; it_m f_n\Phi(\boldsymbol{k}(t_m))e^{-i(2\pi\boldsymbol{k}(t_m)\cdot\boldsymbol{r}_n+\omega_n t_m)}(y_m - [\boldsymbol{A}(\boldsymbol{\omega})\boldsymbol{f}]_m)^{\star}\Big) \\
& + \; \frac{\partial}{\partial \omega_n}\beta_2 R(\boldsymbol{\omega}).
\end{aligned}
\tag{8}
$$

Defining g_n by,

$$
g_n(\boldsymbol{\omega}) = -i\sum_{m=1}^{M} t_m f_n^{\star}\Phi^{\star}(\boldsymbol{k}(t_m))e^{i(2\pi\boldsymbol{k}(t_m)\cdot\boldsymbol{r}_n+\omega_n t_m)}(y_m - [\boldsymbol{A}(\boldsymbol{\omega})\boldsymbol{f}]_m),
\tag{9}
$$

we can formulate the gradients based on the vector $\boldsymbol{g}$ given by,

$$
\boldsymbol{g}(\boldsymbol{\omega}) = -iD(\boldsymbol{f}^{\star})\boldsymbol{A}^{\star}(\boldsymbol{\omega})D(\boldsymbol{t})(\boldsymbol{y} - \boldsymbol{A}(\boldsymbol{\omega})\boldsymbol{f}),
\tag{10}
$$

where $D(\boldsymbol{x})$ denotes a diagonal matrix with the elements of the vector $\boldsymbol{x}$ on its diagonal. Inserting the vector $\boldsymbol{g}$ and using our chosen regularization function $R(\boldsymbol{\omega})$, we can express the gradient of Ψ with

respect to $\boldsymbol{\omega}$ as follows:

$$\begin{aligned}
\nabla_{\boldsymbol{\omega}}\Psi &= \frac{1}{2}(\boldsymbol{g}(\boldsymbol{\omega}) + \boldsymbol{g}^{\star}(\boldsymbol{\omega})) + \beta_2 C'C\boldsymbol{\omega} \\
&= \mathrm{Real}\{\boldsymbol{g}(\boldsymbol{\omega})\} + \beta_2 C'C\boldsymbol{\omega},
\end{aligned} \tag{11}$$

Using the gradient in Eq. (11), we update our estimate of the field map, $\boldsymbol{\omega}^k$, by gradient descent,

$$\boldsymbol{\omega}^{k+1} = \boldsymbol{\omega}^k - \alpha\left(\mathrm{Real}\{\boldsymbol{g}(\boldsymbol{\omega}^k)\} + \beta_2 C'C\boldsymbol{\omega}^k\right). \tag{12}$$

The step size α is chosen such that the cost function, Ψ, decreases.

3   Methods

In principle, one could apply the estimation method described above to any k-space trajectory. However, the quality of the results will certainly be trajectory dependent. The spiral-in/ spiral-out sequence was chosen because it provides efficient coverage of k-space and a close spacing of echo times. A spiral-in/ spiral-out pulse sequence was used in simulation, phantom, and human experiments with the following parameters: TE/FA/FOV = 30ms/60°/24cm, Matrix size = 64×64, and a 1 ms gap between the end of the spiral-in part of the pulse sequence and the beginning of the spiral-out portion. All field-corrected image reconstructions were performed using the fast, iterative technique of [12] on the entire spiral-in/ spiral-out data. This was done so that differences in the reconstructed images can only be due to differences in the field maps and not differences in the reconstruction or regularization. The uncorrected images were reconstructed using a fast gridding operation on the spiral-in and spiral-out portions separately. The resulting images were then combined via a square root of the average of the squares of the images. The computations of $\boldsymbol{Ax}$ and $\boldsymbol{A}^{\star}\boldsymbol{y}$ in Eq. (10) were carried out using the NUFFT and time segmentation algorithms described in [12, 13] with $L = 8$ for time segmentation and a 5×5 neighborhood size and two times oversampling for the NUFFT. Standard estimates for the field maps are usually smoothed to reduce noise. We performed a small amount of smoothing of the standard field map estimates within the object being imaged along with extending the field map beyond the object using a penalized weighted least squares smoothing function [15]. A single iteration of our joint estimation algorithm consisted of both an update of the image (15 iterations of CG algorithm) and the field map (4 iterations of gradient descent).

3.1 Simulation Study

Simulation data sets were formed from a high resolution brain scan with its associated field map at a matrix size of $256 \times 192 \times 128$ and then reconstructed at a lower resolution, a 64×64 matrix size for the reconstructed slice. Noise was added to the data to give an SNR ($\|\text{data}\|/\|\text{noise}\|$) of approximately 100. Two conditions were tested to ensure that the simultaneous estimation algorithm resulted in stable, accurate estimates of the field map. First, the algorithm was started with an initial estimate of the field map of zero. This was used to test if the algorithm would converge to the correct field map when starting from a distant point. Second, the algorithm was initialized with the standard estimate of the field map. Section 4.4 shows that the standard method cannot produce an accurate field map estimate using only the data from a single spiral-in/ spiral-out acquisition. For the standard estimate, an additional scan had to be simulated at an echo time delayed by 2 ms. We used the average of the standard field maps from the spiral-in sequence at the two echo times and the spiral-out sequence at the two echo times as the standard field map. This convention was used both in the simulations and in the phantom and human experiments. We examined the performance of our joint estimation over iteration using the root-mean-squared (RMS) error from the true field map.

3.2 Phantom Study

Next we performed a phantom study using a GE 3T Signa Scanner (GE Medical Systems, Milwaukee, WI). Since the true field map is not known for real data experiments, we obtained a relatively undistorted estimate by acquiring two short echo time four-shot spiral-out images and used the standard field map estimation. This estimate was compared quantitatively to the estimates from the standard estimation and our joint estimation on the spiral-in/ spiral-out data. The resulting images, reconstructed using either the standard field map or the jointly estimated field map were compared qualitatively for reduction in artifact. Since our joint estimation algorithm allows us to estimate a field map for each acquisition, we applied our technique to a time series collected on the phantom using a TR of 2 s and 80 time points. We examined the time course of the field map for a pixel inside the phantom to assess the stability of our estimates.

3.3 Human Studies

The human data sets were collected on a GE 3T Signa Scanner in accordance with the Institutional Review Board of the University of Michigan. Three normal human subjects performed a functional task consisting of 4 cycles of on/off bilateral finger tapping, each cycle lasting 40 seconds. The subjects were instructed to keep their head still during the functional studies. One human study, Subject 1, was performed with a TR of 2 s, yielding 80 time points. Two other human subjects, Subjects 2 and 3, were acquired with a TR of 0.5 s to allow for good resolution of the respiratory waveform which causes small shifts in the field map of axial slices. A respiratory bellows was used to acquire the respiratory waveform for these two subjects. Reconstructions using the dynamic, jointly estimated field maps were qualitatively compared to the reconstructions using the static, standard estimates of the field maps. Also, functional results using the time series of images reconstructed with each field map estimate were compared using the number of active voxels at a given threshold, *i.e.* the number of voxels with a correlation coefficient with the sinusoidal task waveform that exceeded a given threshold. The time series of the field map estimates were also examined for pixels inside the brain. A correlation test was performed to see if the proposed joint estimation method accurately reflected the respiration-induced phase variations.

4 Results

4.1 Simulation Study

Figure 1 shows the axial and sagittal slices used in the simulations and their associated field maps. Figures 2 and 3 show the root-mean square (RMS) error over iteration for the axial study and sagittal study, respectively, for both initialization conditions that were discussed in Section 3.1. Both of these sets of curves show that the simultaneous estimation algorithm converges quickly, in around 50 iterations. Stability of the joint estimation method is also shown by these figures, *i.e.* when the algorithm is started with an estimate close to the local minimum, it stays near that minimum. This suggests that an efficient way to implement the simultaneous estimation algorithm for time series data is to initialize the field map at each time point with the standard, static estimate of the field map and run just a few iterations to account for dynamic changes. When initialized with the standard estimate, Figure 3 shows that the local minimum for the simultaneous estimation has slightly higher RMS error than the standard estimate

at convergence. This is due to a local minimum. Figure 4 shows the map of the error in the estimate. Comparing this error to the sagittal slice in Figure 1, we can see that the error occurs near a peak in the field map at the edge of the object. A regularization scheme other than quadratic, such as a Huber penalty [16] or a spatially varying penalty [17], may improve estimation in those regions.

4.2 Phantom Study

A phantom data set was collected with 80 time points as described in Section 3.2. To estimate the field map with little field-induced distortions, we acquired an extra data set using a 4-shot spiral-out sequence with an echo time of 4.6 ms. The joint estimation algorithm was initialized at each time point with the static, standard estimate of the field map from the spiral-in/ spiral-out data and 50 iterations were performed. Figure 5 shows the field map estimated from this 4-shot, short echo time acquisition along with the standard and jointly estimated field maps using the spiral-in/ spiral-out data. In this case, all three estimated field maps should look similar since the phantom is immobile and has no physiologically induced phase variations or motion. For this slice, we calculated root mean squared difference between the 4 shot field map and the estimated field maps over the object region as defined by the 4-shot image. The RMS difference for the standard estimate was 2.9 Hz and for the jointly estimated field map was 4.3 Hz at time point 2. Recall that the standard field map estimate is an average of the field maps determined from the spiral-in and spiral-out portions of the data at both the first and second time points in the acquisition (Section 3.1). However, the joint estimation used only the data from a single spiral-in/ spiral-out acquisition, although in this case, we are using the standard estimate to initialize the algorithm. Figure 6 shows the resulting images reconstructed with the 4-shot field map, the standard field map and the jointly estimated field map. Since the 4-shot image had a much shorter echo time, it has different T_2^*-weighting. The jointly estimated image and standard image result in similar reconstructions for this phantom study.

We can examine the time course of the dynamic, jointly estimated field map at a pixel of interest to study the variance of our field map estimate and identify any main field drift in the scanner. Figure 7 shows the time course of the field map estimate of a point in the interior of the upper region of the phantom. From this plot we can see that there is a smooth drift of the main magnetic field over the course of the time series, around 2.5 Hz over the 160 s scan time. A similar drift in the field map

11

was seen for all pixels inside the phantom. Such field drifts are seen routinely in our stability scans, possibly due to heating of the passive shim coils. After regressing out a second order polynomial fit to the curve, the residual standard deviation of the estimate averaged over the phantom was 0.12 Hz. Thus our estimation algorithm is fairly stable over the course of a time series and dynamic estimation allowed us to track a 1 Hz/min drift in the main field strength.

4.3   Human Study

A data set was collected during a functional experiment as described for the human study in Section 3.3 with a TR of 2 s and 80 time points (Subject 1). Field inhomogeneity distortions are generally worse for lower slices of the brain that are closer to the air/tissue interfaces of the sinus cavities. We show results for both a slice low in the brain and a slice containing pixels with significant correlation to the motor task. Figure 8 shows the uncorrected image, the standard and jointly estimated field maps, and the reconstructions using those field maps for a low axial slice at the tenth time point. The T_1-weighted anatomical scan is given for reference. Although the two field maps look similar, the arrows in the reconstructed images indicate positions at which the images show differences in the degree to which inhomogeneity correction was successful. The image reconstructed with the standard field map shows blurring and signal loss at the indicated positions, whereas the increased accuracy of the jointly estimated field map allows for adequate compensation and artifact reduction.

Figure 9 gives the results for the field map estimations and the reconstructed images for a slice containing pixels correlated to the bilateral finger tapping task. The results for the jointly estimated image and field map are shown for the tenth time point. The standard field map differs considerably from the jointly estimated field map for this slice. Along the edge indicated by the arrow, the reconstructed image with the standard field map shows significant blurring due to field inhomogeneity. The jointly estimated field map and image are largely free of this distortion.

The reduced artifacts using the jointly estimated field map are also evident in the functional results. Figure 10 shows the functional results from reconstructions using the standard and dynamic field maps for all three human subjects examined. Panels a.-f. show the functional activation maps thresholded at a correlation coefficient of 0.5. The reference image shown under the functional map is the image reconstructed using the corresponding method. For subject 1 in panels a. and d., both methods show

12

similar activation on the left-hand side, but only the joint-estimation method shows a comparable number of active voxels on the right-hand side. The increased bilateral detection corresponds with the increased artifact correction, see the arrow in Figure 9. Panel g. in Figure 10 shows the number of pixels with correlation coefficients higher than various thresholds for the two reconstructions for Subject 1. The trend seen in panels a. and d. for a threshold of 0.5 holds for all the other thresholds examined, *i.e.* a larger number of activated pixels result from correctly compensating for the undistorted, dynamic field map. Panels b. and d. in Figure 10 show the functional maps for Subject 2 (TR = 0.5 s) and panels c. and e. show the functional maps for Subject 3 (TR = 0.5 s). All maps were thresholded at a correlation coefficient of 0.5. Again we see with both these subjects that accurate compensation for the dynamic, jointly-estimated field map results in a larger number of activated voxels. The plots of number of active voxels versus threshold level for the two subjects are shown in panels h. and i., respectively.

Figure 11 shows the estimated field map for a voxel inside the brain over the the course of the functional study for Subject 1. A field drift over the course of the time series exists in the human data that is similar to that from the phantom scan, a positive shift in the field of about 2.5 Hz over the course of the scan. The field map estimates here have higher oscillations than in the phantom study. Regressing out a second order polynomial fit to the time course shown in Figure 11 gives a residual standard deviation of 0.33 Hz, averaged over the brain.

The higher variance in the time series of the field map from the human study vs the phantom study (Figure 11 vs. 7) could be due to respiration-induced field changes during the course of the time series. To examine this effect further, two of the subjects were scanned with a TR of 0.5 s to allow for good resolution of the respiratory effect and a respiratory bellows was used to acquire the respiration waveform, as described in Section 3.3. We performed a correlation analysis between the measured respiratory waveform and that from the time course of the estimated field map after regressing out a second order polynomial fit to remove the main field drift component. We found that for Subject 2, there was a mean correlation coefficient of 0.39 over the brain region between the field map values (after removing a second order polynomial fit) and the respiratory waveform. For Subject 3, the mean correlation coefficient over the brain was 0.43. A plot of the time course of the field map for a pixel inside the brain of Subject 3 is shown in Figure 12. This pixel was near the center of the brain and had the highest correlation coefficient with the respiratory waveform, 0.80. Also shown in this figure for reference is a scaled version of the respiratory waveform as measured from the respiratory bellows. The variations in the field map

values are a good fit to the scaled measurements from the respiratory bellows.

4.4   Non-iterative Dynamic Estimation

At first glance, it might appear that a dynamic field map estimate could be formed by first reconstructing uncorrected images from the spiral-in and spiral-out parts of the sequence separately. These acquisitions were spaced by 1 ms in our studies, so the field map could be formed by taking the phase difference of these two images and dividing by the difference in echo times. Figure 13 shows the field maps estimated in this manner for the simulation and phantom experiments. These field maps have shapes that are fairly consistent with the truth (refer to Figures 1 and 5), but the scaling is wrong, even resulting in phase wraps in the field map. The problem with this non-iterative dynamic method is that the point spread function of a spiral-in sequence with field inhomogeneity differs greatly from that of a spiral-out acquisition. A possible explanation is offered in [18]: gradients in the field map distort the local k-space trajectory which may cause a shift in the timing of the sampling of the center of k-space, the effective echo time, that may differ greatly from the planned echo time. In the usual case, when comparing spiral-out sequences of the same slice at two different echo times, this effective echo time shift is the same for both, keeping the difference in effective echo times the same as the planned echo time delay. However, the time at which the origin of k-space is sampled for spiral-in and spiral-out sequences is affected differently by gradients in the field map. This results in an effective difference in echo time between the spiral-in and spiral-out sequences that varies spatially. Hence, in addition to the usual problems associated with the standard field map estimate discussed in Section 1, the field map estimates are also degraded by a space-variant scale factor.

5   Discussion

The simulation studies show that our joint estimation technique can estimate a field map that is similar in accuracy to the standard field map estimate. The standard field map estimate requires two acquisitions at slightly different echo times and assumes that the field map remains static over the course of a time series. Our joint estimation technique uses a spiral-in/ spiral-out sequence to estimate an undistorted field map and image at each acquisition. This dynamic estimate was formed using a penalized, least-

14

squares joint-estimation algorithm and a spiral-in/ spiral-out acquisition, which does not decrease the scan efficiency from a spiral-out sequence.

The jointly estimated field map is very stable. For each time point, the dynamic estimation is started with the static, standard estimate of the field map from the first two time points and an initial estimate of zeros for the image. That means that each time point is initialized with the same image and field map and is not dependent on the time points around it. So, by looking at the variance in the time series of the estimated field maps, we can examine the stability of the estimations. In the phantom experiment, the average standard deviation for the time course of the field map was only 0.12 Hz after removing trends to account for the drift of the magnetic field. The mean standard deviation from the human results was 0.33 Hz. This higher variation resulted from respiration-induced phase variations during the time series. The time series of pixels inside the brain in a slice from two subjects exhibited significant correlation with the respiratory waveform as measured with a respiratory bellows. A mean correlation coefficient of 0.4 was observed for the time course of the field map with the measured respiratory waveform in a slice high in the brain in two subjects. This respiration effect should be even greater for slices lower in the brain.

For this work, the accurate measurement of respiratory effects in the time course of the field map attests to the stability and sensitivity of our method. In subsequent work, the ability of our proposed method to accurately estimate and correct for respiratory noise should be compared to other physiological noise correction schemes. For example, a technique called "dynamic off-resonance in k-space" or DORK assumes that respiration-induced phase is constant over the slice [19]. This assumption essentially restricts the application of DORK to axial slices. Although our method does use spatial regularization, it does not enforce a uniform shift for the slice. Therefore, our method is applicable to any slice orientation.

Besides the fact that the proposed method is able to track dynamic changes in the field map, the human experiments suggest that our method results in a more accurate estimate of a single field map. Although the dynamic changes in the field maps over the time series were relatively small (<5 Hz), the functional results were dramatically different when using the jointly estimated field map instead of the standard field map. The jointly estimated field map resulted in an image with less artifact and a higher number of activated voxels in the functional studies. The standard field map estimation method suffers from the use of reference images that are distorted by field inhomogeneity effects, physiologically-induced phase differences, and motion between the reference images.

The joint estimation algorithm can accurately and dynamically track and correct for changes in the field map during the course of the functional study. These changes may be due to respiration-induced phase changes, head movement, and drifts in the center frequency of the magnetic field. These effects will become even more significant at higher field strengths, so dynamic estimation of the field map may be crucial for success of fMRI at high fields. In this work, the subject was instructed to hold their head still. In patient and pediatric populations, the subject may not be able to remain still for the time required for a functional study. In these cases, dynamic field map estimation may be necessary for adequate artifact correction and proper estimation of motion-correction parameters. In our future work, we will examine the impact of dynamic field map estimation on motion correction.

Our proposed joint estimation algorithm can be used with any pulse sequence that provides adequate sampling of k-space with a diversity in echo times to give information about phase accrual. It has also been used with a four-echo spiral-out sequence to estimate the image, field map and T_2^* relaxation map [20]. The spiral-in/ spiral-out sequence was chosen for this work because it provides an efficient coverage of k-space and allows for a close spacing of echo times. Sub-sampling strategies, such as those using variable-density spirals [9] or radial lines [10], may allow for a reduction in the acquisition time.

One drawback to the proposed method is computation time. On a 2 GHz Pentium workstation running Matlab, 50 iterations of the proposed method to estimate an image and a field map took approximately 20 minutes. Recall that one iteration of our proposed method includes 15 iterations of CG on the image and 4 iterations of gradient descent, see Section 3. Some improvement in computation time will result from optimizing the number of sub-iterations for the image and field map updates. Also, we are using steepest descent for the nonlinear problem of minimizing over the field map, a different minimization algorithm may reduce the total number of iterations required.

6   Conclusion

We have presented a method to accurately estimate an undistorted image and field map for each acquisition of a spiral-in/ spiral-out sequence. This method results in stable field map estimates that are able to track field drift and respiration-induced phase variations over the course of an fMRI time series. Despite producing dynamic estimates, we have shown that our method can result in better single field map estimates in humans than the standard estimation technique, which is sensitive to differences between the

reference images due to subject motion and respiration.

References

[1] S. Ogawa, D. W. Tank, R. Menon, J. M. Ellerman, S.-G. Kim, H. Merkle, and K. Ugurbil, "Intrinsic signal changes accompanying sensory stimulation: Functional brain mapping with magnetic resonance imaging," *Proc Natl Acad Sci*, vol. 89, pp. 5951–5955, 1992.

[2] D. C. Noll, C. H. Meyer, J. M. Pauly, D. G. Nishimura, and A. Macovski, "A homogeneity correction method for magnetic resonance imaging with time-varying gradients," *IEEE Trans. Med. Imag.*, vol. 10, no. 4, pp. 629–637, 1991.

[3] D. C. Noll, J. M. Pauly, C. H. Meyer, D. G. Nishimura, and A. Macovski, "Deblurring for non-2D Fourier transform magnetic resonance imaging," *Magn. Reson. Med.*, vol. 25, pp. 319–333, 1992.

[4] Y. M. Kadah and X. Hu, "Simulated phase evolution rewinding (SPHERE): A technique for reducing B_0 inhomogeneity effects in MR images," *Magn. Reson. Med.*, vol. 38, pp. 615–627, 1997.

[5] H. Schomberg, "Off-resonance correction of MR images," *IEEE Trans. Med. Imag.*, vol. 18, no. 6, pp. 481–495, 1999.

[6] L.-C. Man, J. M. Pauly, and A. Macovski, "Multifrequency interpolation for fast off-resonance correction," *Magn. Reson. Med.*, vol. 37, pp. 785–792, 1997.

[7] E. Schneider and G. Glover, "Rapid in vivo proton shimming," *Magn. Reson. Med.*, vol. 18, pp. 335–347, 1991.

[8] S. J. Peltier and D. C. Noll, "Physiological noise in multi-shot functional MRI," in *ISMRM Tenth Scientific Meeting*, 2002, p. 118.

[9] K. S. Nayak, C.-M. Tsai, C. H. Meyer, and D. G. Nishimura, "Efficient off-resonance correction for spiral imaging," *Magn. Reson. Med.*, vol. 45, pp. 521–524, 2001.

[10] K. S. Nayak and D. G. Nishimura, "Automatic field map generation and off-resonance correction for projection reconstruction imaging," *Magn. Reson. Med.*, vol. 43, pp. 151–154, 2000.

[11] G. H. Glover and C. S. Law, "Spiral in/out BOLD fMRI for increased SNR and reduced suscepti-bility artifacts," *Magn. Reson. Med.*, vol. 46, pp. 515–522, 2001.

[12] B. P. Sutton, D. C. Noll, and J. A. Fessler, "Fast, iterative, field-corrected image reconstruction for MRI," *IEEE Trans. Med. Imag.*, vol. 22, no. 2, pp. 178–188, 2003.

[13] J. A. Fessler and B. P. Sutton, "Nonuniform fast Fourier transforms using min-max interpolation," *IEEE Trans. Signal Processing*, vol. 51, no. 2, pp. 560–574, 2003.

[14] E. M. Haacke, R. W. Brown, M. R. Thompson, and R. Venkatesan, *Magnetic resonance imaging: Physical principles and sequence design*, John Wiley and Sons, New York, 1999.

[15] J. A. Fessler, "Penalized weighted least-squares image reconstruction for positron emission tomog-raphy," *IEEE Trans. Med. Imag.*, vol. 13, no. 2, pp. 290–300, 1994.

[16] P. J. Huber, *Robust statistics*, Wiley, New York, 1981.

[17] J. W. Stayman and J. A. Fessler, "Regularization for uniform spatial resolution properties in penalized-likelihood image reconstruction," *IEEE Trans. Med. Imag.*, vol. 19, no. 6, pp. 601–615, 2000.

[18] D. C. Noll, "Rapid MR image acquisition in the presence of background gradients," in *Proc. IEEE Int. Symp. Biomed. Im.*, 2002, pp. 725–728.

[19] J. Pfeuffer, P.-F. Van de Moortele, K. Ugurbil, X. Hu, and G. H. Glover, "Correction of physiologically-induced global off-resonance effects in dynamic echo-planar and spiral functional imaging," *Magn. Reson. Med.*, vol. 47, pp. 344–353, 2002.

[20] B. Sutton, S. J. Peltier, J. A. Fessler, and D. Noll, "Simultaneous estimation of I_o, R_2^*, and field map using a multi-echo spiral acquisition," in *ISMRM Tenth Scientific Meeting*, 2002, p. 1323.

7 Figures and Tables

a

b

c

d
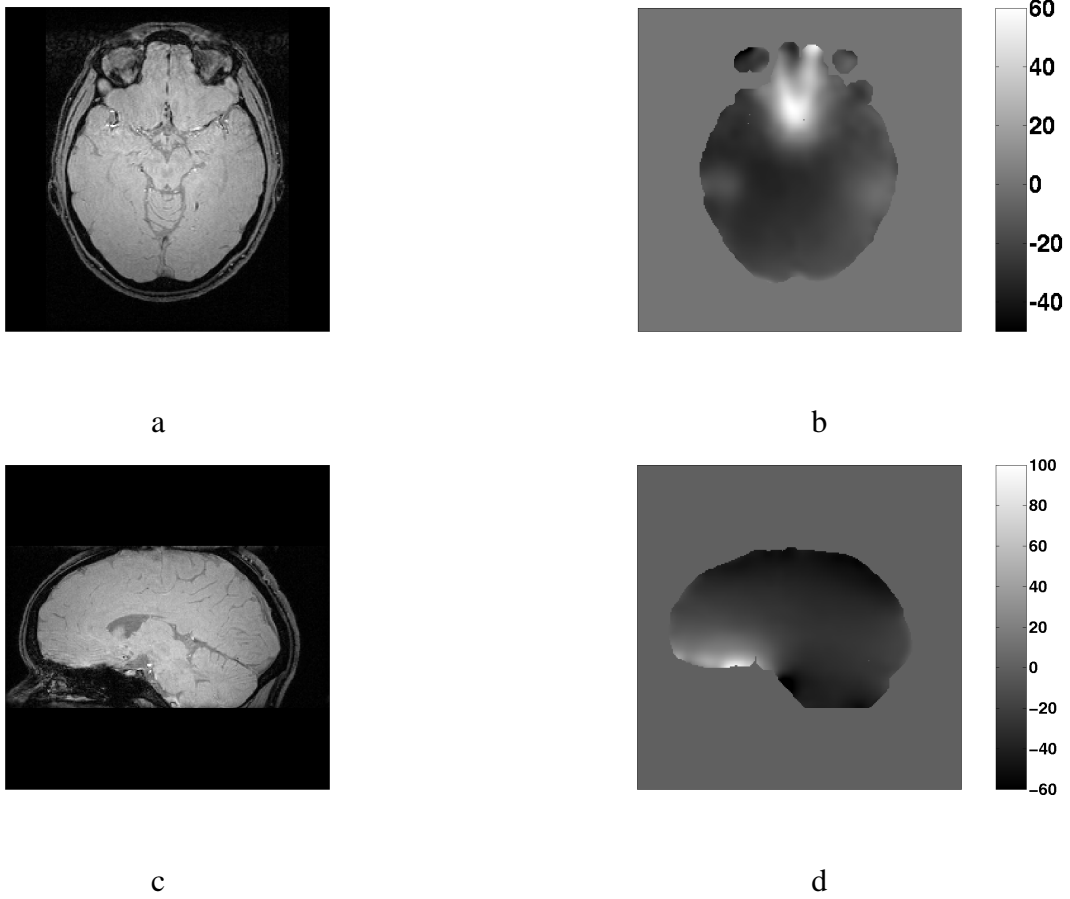
Figure 1: Objects used for simulation study. a.) axial slice b.) axial field map (Hz) c.) sagittal slice d.) sagittal field map (Hz)
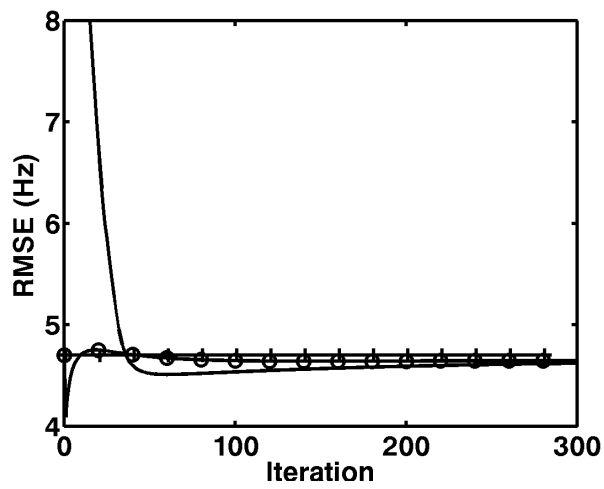
Figure 2: RMS error in Hz vs iteration number for the axial slice simulation. Solid line (-) is the simultaneous estimation initialized with a zero field map, Circles (o) are the simultaneous estimation initialized with the standard field map, Plus (+) is the standard field map estimate, which is not iterative but is shown as a constant value vs iteration.
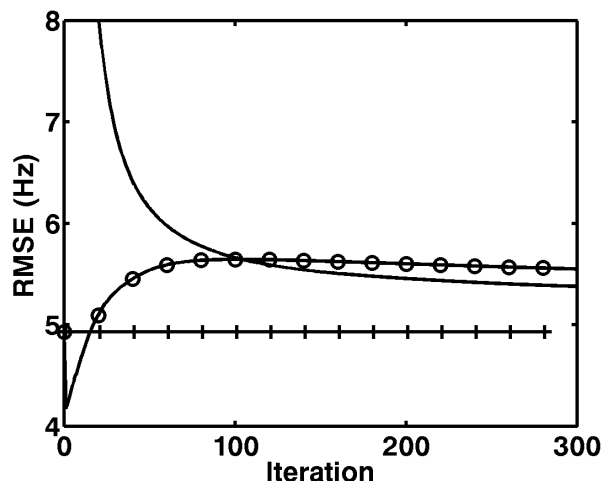
Figure 3: RMS error in Hz for the sagittal slice simulation. Solid line (-) is the simultaneous estimation initialized with a zero field map, Circles (o) are the simultaneous estimation initialized with the standard field map, Plus (+) is the standard field map estimate, which is not iterative but is shown as a constant value vs iteration.
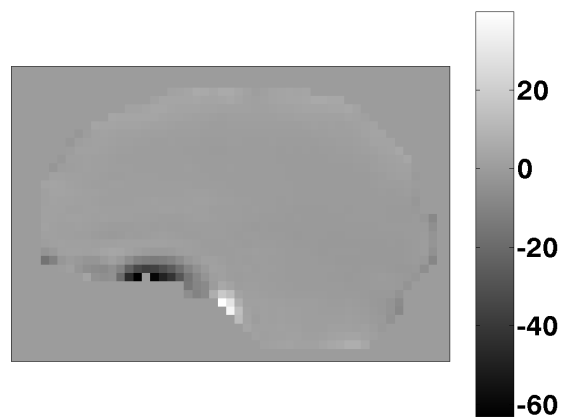
Figure 4: Error in Hz for the sagittal slice.
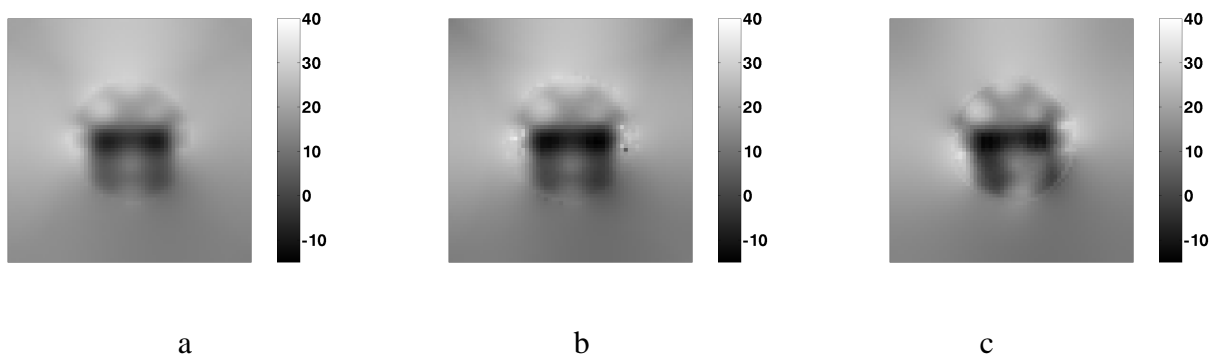
Figure 5: Field maps for the phantom study in Hz: a.) 4-shot short echo time spiral-out with standard field map estimation, b.) standard field map estimate c.) jointly estimated field map.
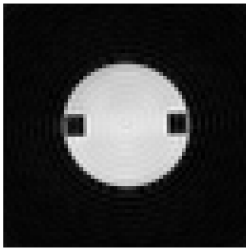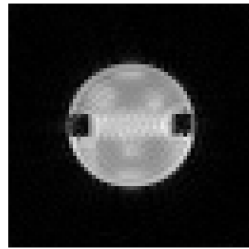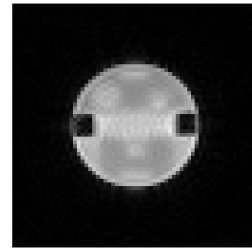
Figure 6: Reconstructions from phantom experiment: a.) 4-shot short echo time spiral-out, b.) spiral-in/ spiral-out using the standard field map estimate c.) spiral-in/ spiral-out using the jointly estimated field map.
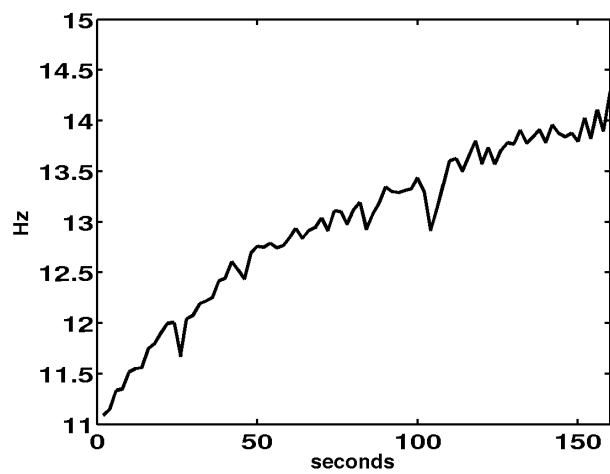
Figure 7: Time course of the jointly estimated field map for a pixel inside the phantom.

a b c

d e f
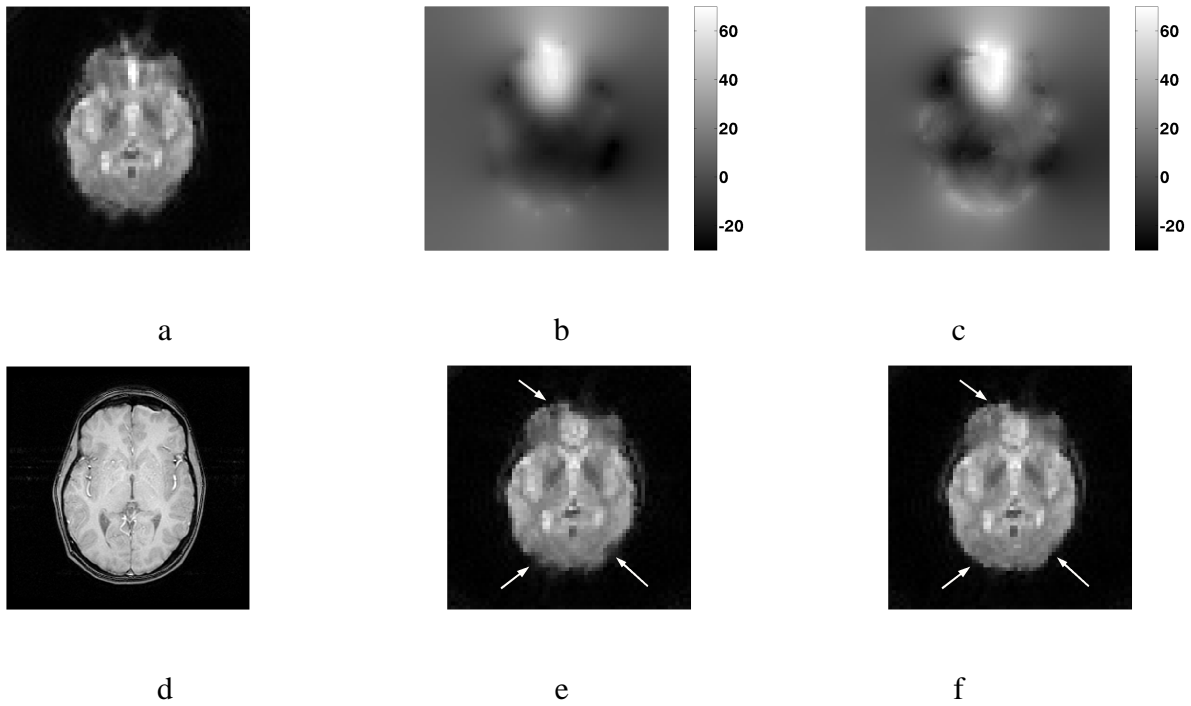
Figure 8: Results of reconstruction and estimation on a slice lower in the brain of Subject 1. a.) uncorrected image, b.) standard field map estimate, c.) jointly estimated field map, d.) T_1 anatomical image for reference e.) image reconstructed using the standard field map, f.) image reconstructed using the jointly estimated field map.
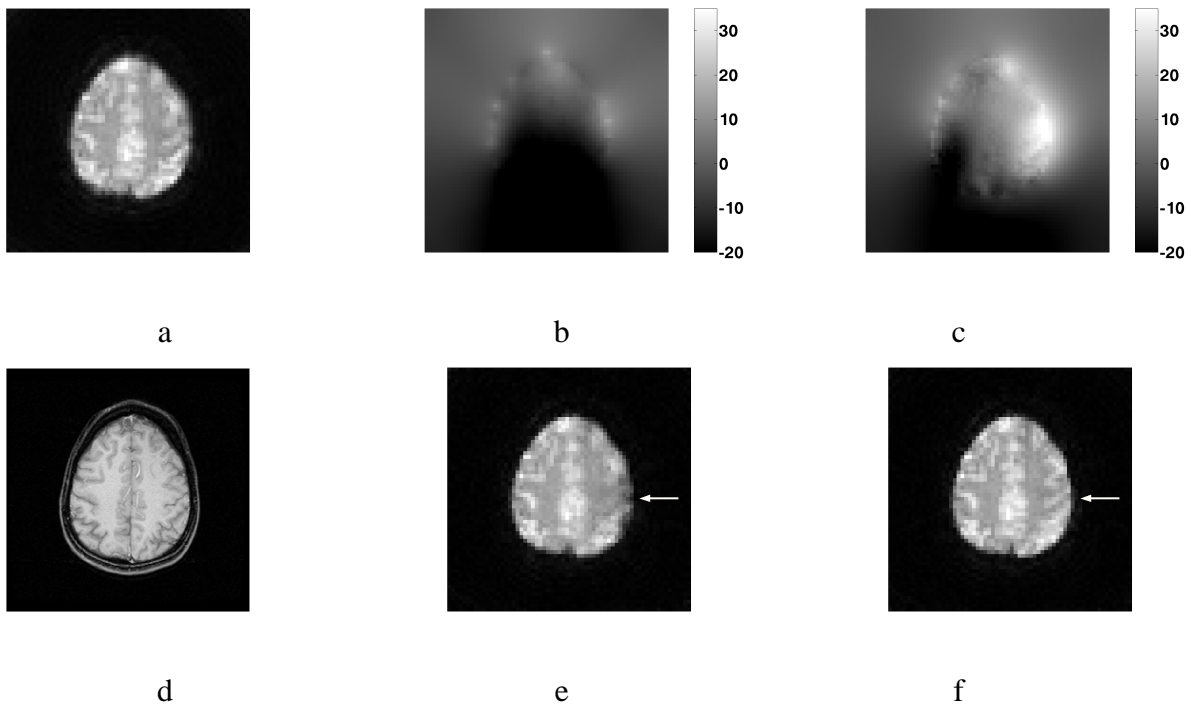
Figure 9: Results of reconstruction and estimation on slice of interest for functional study for Subject 1. a.) uncorrected image, b.) standard field map estimate, c.) jointly estimated field map, d.) T_1 anatomical image for reference e.) image reconstructed using the standard field map, f.) image reconstructed using the jointly estimated field map.
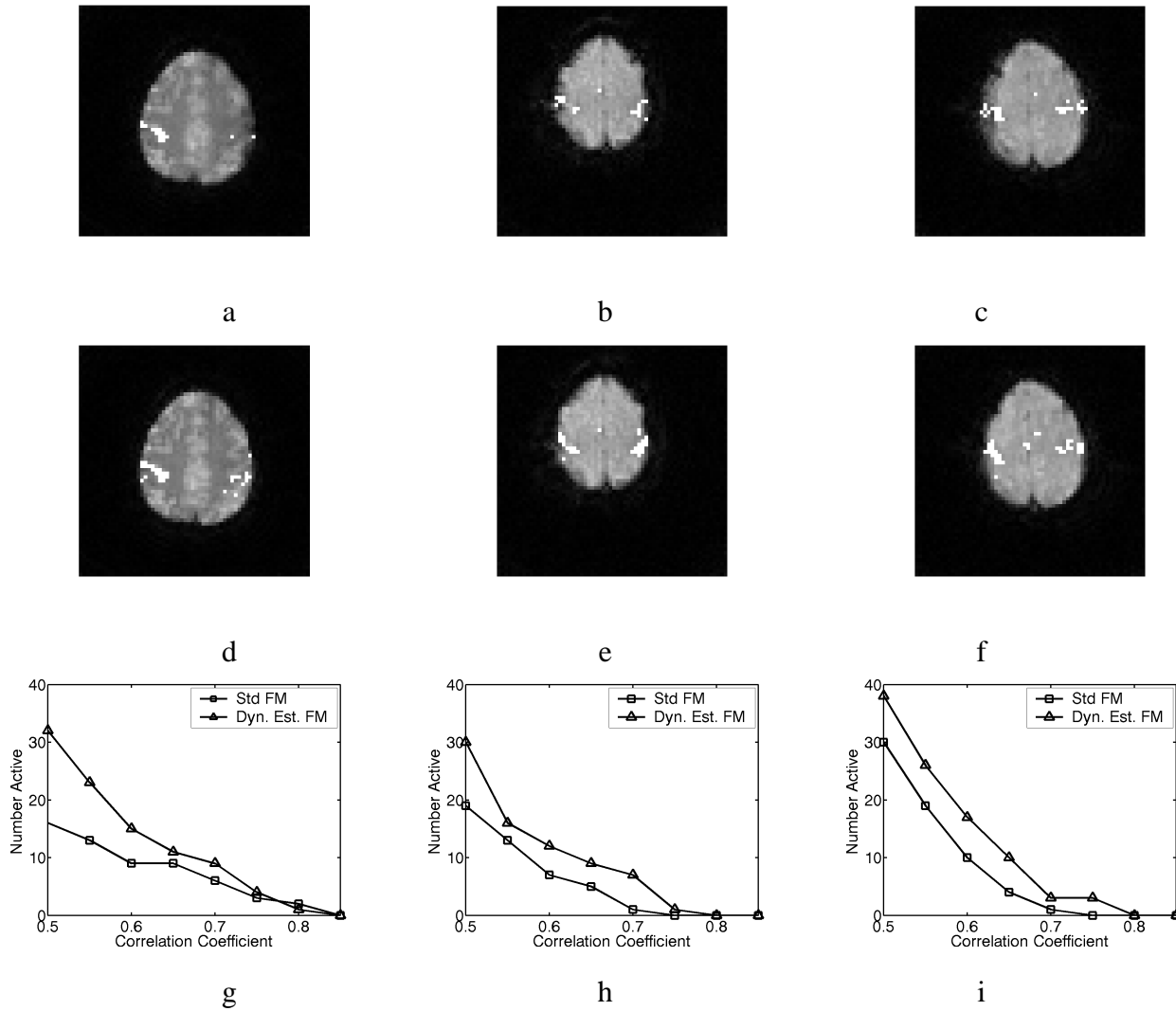
Figure 10: Functional results for the two reconstructions for all three human subjects. Reconstruction using the standard field map for: a.) Subject 1, b.) Subject 2, c.) Subject 3. Reconstruction using the jointly estimated field map for d.) Subject 1, e.) Subject 2, f.) Subject 3. Plot of number of pixels with correlation coefficients higher than the threshold for various thresholds for g.) Subject 1, h.) Subject 2, i.) Subject 3.
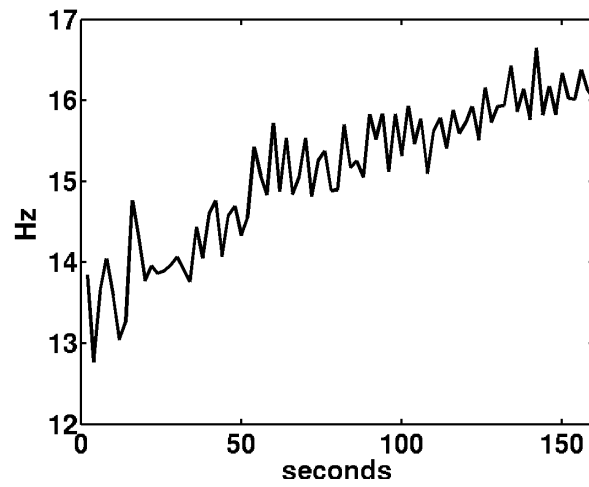
Figure 11: Time course of simultaneously estimated field map for a pixel within the brain.
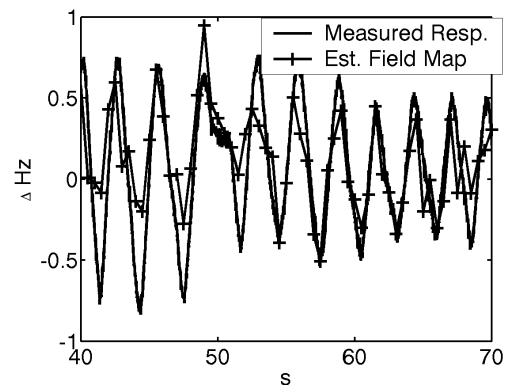
Figure 12: Plot of time course of field map for a pixel inside the brain of Subject 3 after regressing out a second order polynomial fit to remove the main field drift component. Shown also for reference is a scaled version of the waveform measured from the respiratory bellows.
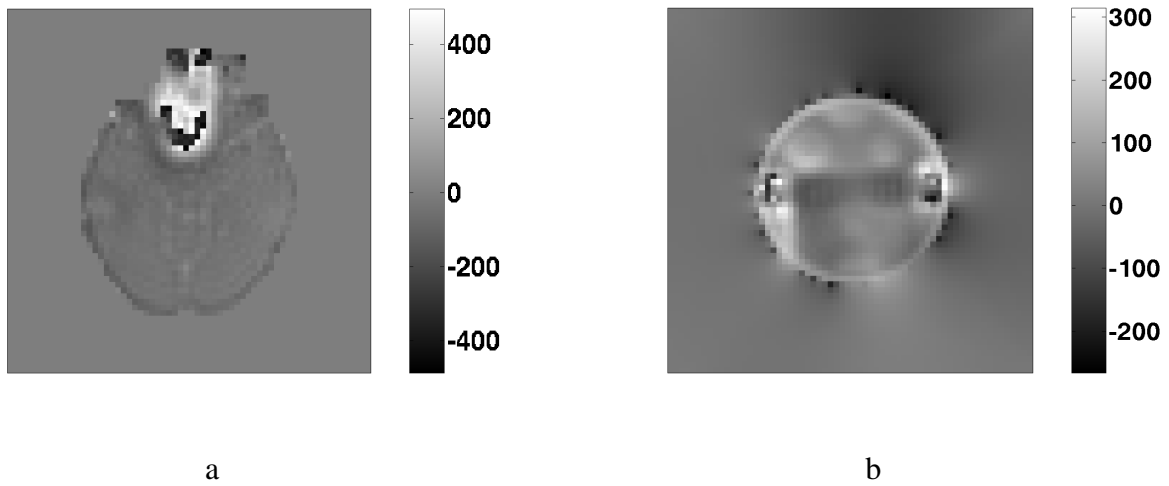
Figure 13: Field maps estimated from the phase differences of spiral-in and spiral-out images reconstructed separately. a.) simulation field map (Hz), b.) phantom field map (Hz).